

FULL ARTICLE

Fast non-negative temporal deconvolution for laser scanning microscopy

Kaspar Podgorski and Kurt Haas*

Department of Cellular and Physiological Sciences and the Brain Research Centre, University of British Columbia, 2211 Wesbrook Mall, Vancouver, BC, V6T2B5, Canada

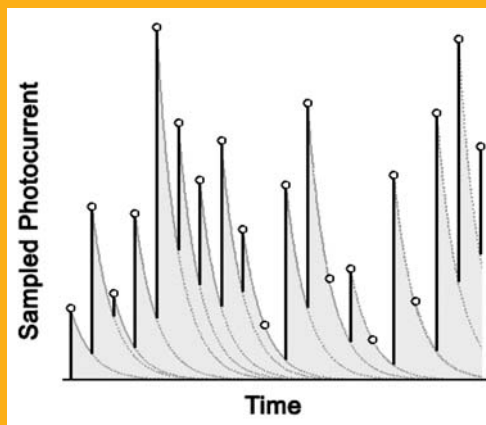
Received 6 December 2011, revised 27 February 2012, accepted 28 February 2012
Published online 22 March 2012

Key words: two-photon, image acquisition, algorithms, calcium imaging

➔ **Supporting information** for this article is available free of charge under <http://dx.doi.org/10.1002/jbio.201100133>

Laser scanning microscopy (LSM) is a common technique for high resolution fluorescent imaging. Here we describe a fast algorithm for non-negative deconvolution and apply it to readout of LSM detector photocurrents. By broadening photon impulses and deconvolving sampled photocurrent, effective quantum efficiency of the imaging system is increased. Using simulation and imaging with a custom-built two-photon microscope, we demonstrate improved fidelity of images acquired at short dwell times over a wide range of photon rates. Images formed show increased correlation-to-sample equivalent to a 25% increase in photon rate, lower noise, and reduced bleed-through compared to conventional image generation.

Abstract Figure: Deconvolution of an exponential decay kernel from a sampled signal. The contribution of decaying signal from each sample to subsequent samples is predicted and cancelled out. This principle can be used to improve measurements in laser scanning microscopy,



where pixel intensities are acquired serially. This simplified trace lacks noise; we present a fast algorithm for least-squares optimal deconvolution in the presence of noise. The algorithm shows further application for fast spike inference from neuronal calcium imaging.

1. Introduction

Fluorescence microscopy has become a leading tool for investigating cellular and systems biology, allowing imaging of labeled structures and molecules with subcellular resolution. Genetically encoded fluorescent proteins [1] have revolutionized our understanding of fundamental biological processes on

scales ranging from protein interactions [2], to cellular structure [3], to entire tissues [4]. Quantitative imaging of fluorescent sensors has allowed continuous, spatially resolved monitoring of cellular signaling, complementing or replacing more invasive techniques and enabling studies in awake animals [5, 6].

Laser scanning confocal and multi-photon microscopy (LSM) allow high resolution fluorescence imag-

* Corresponding author: e-mail: kurt.haas@ubc.ca, Phone: 604-822-9770, Fax: 604-822-7299

ing by collecting light from a single focal plane, and have become dominant techniques in this field [7]. In LSM, a focused laser beam is scanned in two or three dimensions through a sample, and fluorescence emitted by the sample is collected and typically focused onto a single photodetector, which reads out photons for each pixel in sequence. Because pixels are acquired in sequence, little time is available to sample each pixel, particularly when the imaging area is large, the sample rate is high, or the image must be of high fidelity. Such conditions are common in biological experiments, and most applications thus require that photons be detected by the imaging system at a high rate, so that pixel brightness can be accurately measured in a short amount of time. This need for high photon rates has motivated the development of bright fluorescent dyes [8] and highly efficient photodetectors used in current imaging applications.

Efficient signal processing and image generation are also important to LSM, and the manner in which photodetector signals are conditioned and processed can dramatically impact the sensitivity and dynamic range of the imaging system. Signal processing is particularly important in quantitative imaging, where pixel brightness must be measured with high precision, and systematic errors can bias experimental results. Here we introduce a signal processing method, non-negative deconvolution (NND), which improves LSM performance over a wide dynamic range. We compare NND to conventional deconvolution and to two existing methods, photon counting and photocurrent binning.

As LSM equipment has become readily available, many investigators have built custom microscopes designed to address specific research questions or as lower-cost alternatives to commercial systems [9–11]. The flexibility of such custom systems allows researchers to rapidly implement new signal processing methods such as the one described here. With such researchers in mind, an optimized form of the NND algorithm is available upon request.

1.1 Photon counting

Photomultiplier tubes, the detectors most commonly used in LSM, are sensitive enough to resolve impulses due to single photons. When the photon rate is low, these distinct pulses can be counted by a discriminator to produce a sequence of photon arrival times (Figure 1a). This is an effective method for measuring sample brightness provided that impulses are sufficiently separated in time to be discriminated. When photon rates are higher, however, photon counters exhibit saturation as impulses become increasingly likely to overlap in time. As a result, photon counting is most effective at lower count

rates, and commercially available photon counting systems exhibit maximum useful count rates on the order of 10 Mhz. Multipixel photon counting devices [12], superconducting detectors [13], and avalanche photodiodes [14] have been developed that enable higher count rates and promise to replace PMTs as the detectors of choice for LSM applications. However, high quantum efficiency PMTs remain the most effective commercially available detectors for rapid LSM imaging due to their combination of low noise and efficient photon detection. A recently developed

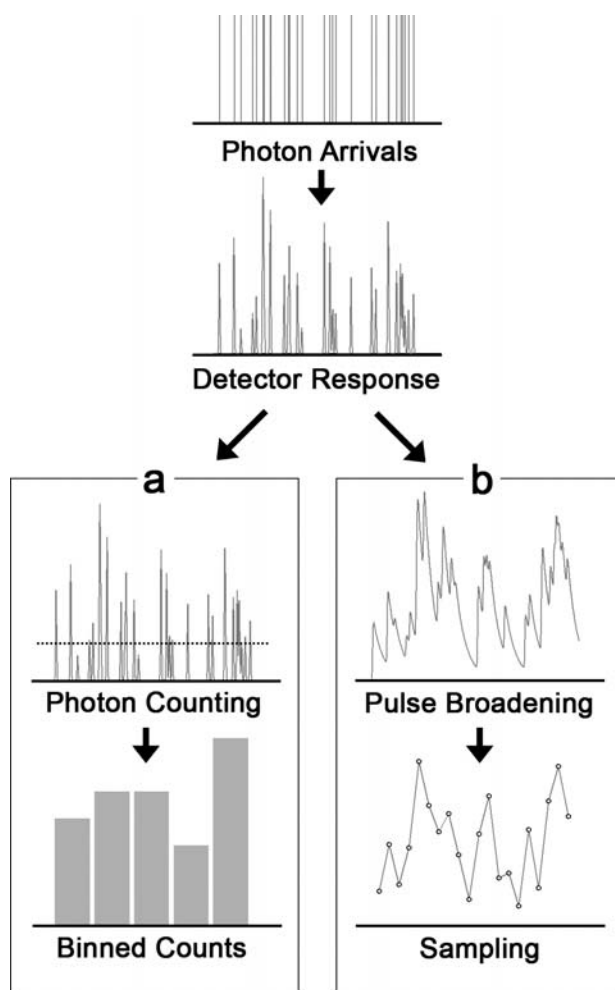


Figure 1 Methods for measuring photon rates in LSM. Photons striking a photomultiplier tube (top) result in responses that can be processed in two ways. **(a)** In Photon Counting, the PMT current is passed through a discriminator which detects threshold crossings. By doing so, variability in pulse amplitudes is removed, but pulses arriving too close in time are registered as one pulse, and low amplitude pulses are missed. **(b)** Analog Measurement. Photon pulses are broadened, and the resulting photocurrent is digitized at a fixed sampling rate. Pulse height variability contributes to measurement noise, but high photon rates can be detected.

PMT-based system for two-photon LSM, using a high-speed complex programmable logic device for counting, is effective at count rates above 100 MHz [15].

At the pixel dwell times and light levels at which photon counting is most effective, imaging fidelity is strongly limited by the Poisson statistics of photon emission. This noise can only be overcome by increasing the photon detection rate, either by increasing the brightness of the sample or the efficiency of the detection system.

1.2 Photocurrent measurement

At higher photon rates, detector impulses begin to overlap to the point that individual photons can no longer be easily discriminated and merge into a sum photocurrent. The larger number of incident photons contributing to the photocurrent reduces the relative contribution of Poisson noise to light measurements, improving the fidelity of the detection system. Photocurrent is typically sampled at a fixed rate using an analog-to-digital converter (ADC), and this readout is used to reconstruct the time-varying

photon rate. Photocurrent measurement does not inherently produce a sequence of photon arrival times, and care must be taken when generating an image from these samples to avoid introducing errors.

A common method to generate LSM images is photocurrent binning, which defines the brightness of each pixel as the average sampled photocurrent over an appropriate time window (Figure 2a). This method introduces error into resulting images due to the finite sampling rate of ADCs used in LSM systems. At the high bit depth required to accurately digitize photocurrent, commonly used ADCs operate at 1–5 MHz, not much faster than pixel dwell times typical for fast imaging applications ($\sim 2 \mu\text{s}$) [10]. To be measurable at slower sample rates, photon pulses produced by the PMT must be expanded in time. This is done by increasing termination resistance to slow the exponential decay of pulses in high capacitance detectors. The breadth of pulses is selected to compromise between two sources of error. Narrow pulses result in sampling-induced variability, which arises because the total signal measured from a pulse depends on its onset time relative to the sample clock (Figure 2b, c). This variability, which decreases the effective quantum efficiency of the imaging sys-

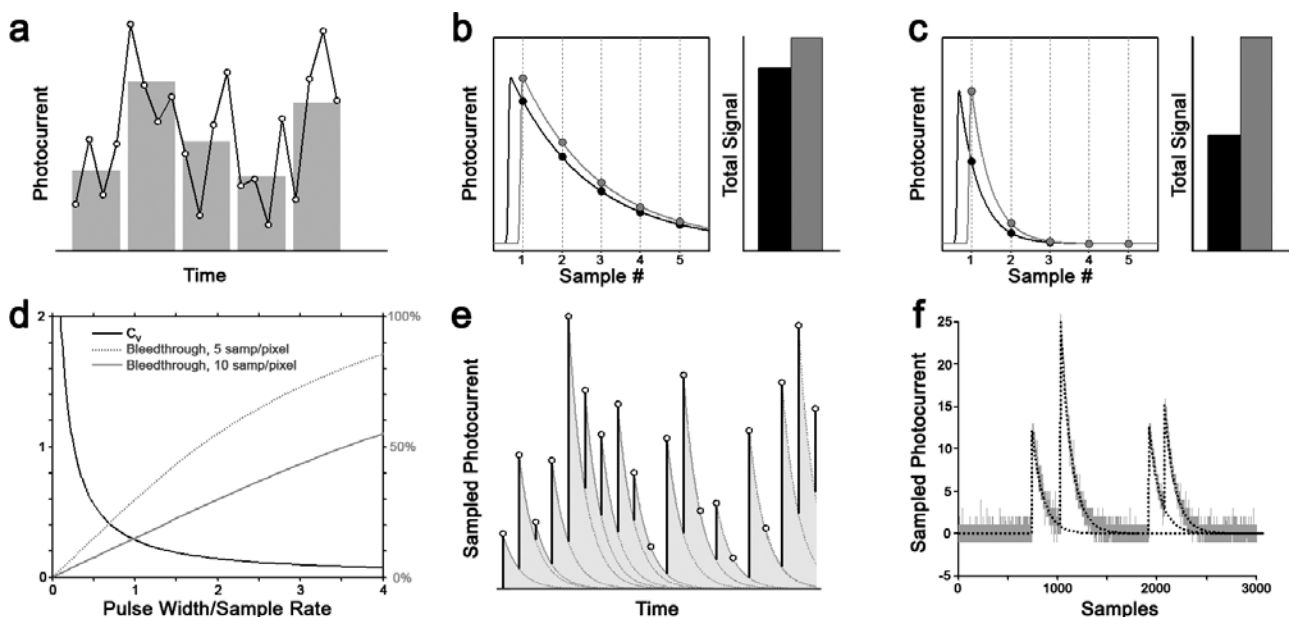


Figure 2. (a) In Photocurrent Binning, photocurrent samples are averaged over time to generate an intensity for each pixel in the image. (b, c) The accuracy with which current pulses are measured depends on the ratio of the pulse width to the sampling interval. When pulses are short (c), the signal produced by a photon varies more strongly with time of arrival relative to the sample clock, than when pulses are long (b). (d) Coefficient of variation (left axis) and percent bleedthrough (right axis) for different pulsewidth/samplerate ratios, with a pixel dwell time of 5 or 10 ADC samples. At ratios which result in high effective quantum efficiency, bleedthrough between adjacent pixels is strong. (e) In Nonnegative Deconvolution, the contribution of decaying photocurrent from each sample (black circles, same values as in (a)) to subsequent samples is predicted (grey curves) and cancelled out, removing bleedthrough. The corrected values (vertical black lines) can then be binned to obtain an intensity for each pixel. Noise has been omitted for clarity. (f) Photocurrent trace recorded from a photomultiplier tube. The trace can be fit very accurately as a sum of exponential decay transients displaced in time, showing that photon pulses add linearly.

tem, can be quantified as the ratio of the standard deviation to the mean of single-pulse measurements (the coefficient of variation, CV). Broad pulses have reduced variability, but decay slowly, leading to bleed-through between pixels. At sample rates and pixel dwell times used for real-time quantitative imaging, pulse breadths which produce a low CV (and thus a high effective quantum efficiency) result in considerable bleed-through between adjacent pixels when using photocurrent binning (Figure 2d).

1.3 Non-negative deconvolution (NND)

Here we describe an alternate method to generate images from sampled photocurrent. To avoid the limitations of binning, we allow pulses to be broad, ensuring high effective quantum efficiency, and infer the photon rate in a way that avoids the problem of bleed-through.

Because photon pulses add linearly (Figure 2f), we treat the photocurrent as the superposition of many single pulses displaced in time. The sampled detector output x can thus be described as the discrete time convolution of a known single-photon impulse response h with the time-varying photon rate s :

$$x(t) = \sum_{\tau} (h(\tau) \cdot s(t - \tau)) + n(t) \quad (1)$$

where n is additive noise. We do not include a term for variations in the height of individual pulses. Because photons add linearly and the photon rate s is real-valued, one cannot distinguish two photons arriving simultaneously from a single photon generating a pulse twice as large. Pulse height variations thus contribute to measurement noise but do not affect the inference procedure.

To best construct the image we must accurately infer s , the photon rate at each sample interval, which is always non-negative. This problem is known as non-negative deconvolution (NND), and can be formalized for a least squares estimator:

$$\arg \min_{\hat{s}_k \in \mathbb{R}_0^+ \forall k} \sum_t (x(t) - \hat{x}(t))^2 \quad (2)$$

where \hat{x} is the following discrete time convolution:

$$\hat{x}(t) = \sum_{\tau} h(\tau) \cdot \hat{s}(t - \tau) \quad (3)$$

Several approaches exist to solve this or other formulations of the NND problem [16–18]. However, general algorithms execute too slowly to be practical at the high data rates attained with LSM. Because of unique properties of the PMT impulse response function h , we are able to solve the NND problem efficiently with complexity $O(n)$ (see Supplementary Information).

Using NND to solve for the photon rate has two potential advantages over photocurrent binning. NND uses a long time course of the detector signal to estimate the photon rate at each point. This large number of samples reduces the effects of measurement noise on the resulting image. NND also allows pulses to be broad without causing bleedthrough effects, removing the need to compromise between these factors in selecting the pulse width.

If the non-negative constraint on the photon rate is removed, and the spectral properties of the noise can be estimated, the NND problem turns into Wiener deconvolution (WD) [19]. This method shares benefits with NND, removes bleedthrough, and can be performed quickly in the Fourier domain with highly optimized algorithms [20], but may be more sensitive to noise due to the ability to fit negative values of s .

2. Methods

2.1 Simulations

Simulations were coded in Matlab (Mathworks, Natick, MA), and all code used for simulations is available upon request. For simulations of imaging, the detection of photons was treated as a heterogeneous Poisson process with time-varying photon rate defined by the pixel intensity, producing a sequence of arrival times t_i . The photocurrent I_P was generated by first assigning each photon a normal random intensity a_i ($\mu = 1$, $\sigma = 0.3$; negative intensities were discarded). This intensity distribution approximates the single-electron response spread of a PMT obtained using oscilloscope measurements. The randomly generated photon point process was then convolved with the impulse response function h scaled by a_i :

$$I_P(t) = \sum_i a_i \cdot h(t - t_i)$$

$$h(x) = H(x) \cdot e^{-x/\tau}$$

Where H is the Heaviside step function. The time constants (τ) used for photocurrent binning and NND differed and were chosen to optimize the performance of each method (NND, $\tau = 441$ samples; photocurrent binning, $\tau = 0.8$ samples). These time constants were varied in simulations in Figure 4a. To simulate digitization by the ADC, this function was sampled at a fixed interval with a small amount ($\sigma = 0.1$) of Gaussian noise added, and digitized at 12 bits. This measurement noise reflects the 0.5 bit RMS dither present in most DAQ cards as well as amplifier noise, and is a lower bound on noise levels achievable for typical samples with 12 bit digitiza-

tion. Noise levels were varied in simulations in Figure 4b. Photon counter properties (pulse-pair resolution, discrimination threshold) used in simulations were based upon specifications of the H7421-40 photon counting module (Hamamatsu Photonics, Japan).

Simulations in Figure S1 were performed using a slightly different model (described in [15]), involving a repeating ultrafast laser (rate, 75 MHz) producing a Poisson-distributed number of photons arriving according to the fluorescence decay (4.1 ns) of a dye. Counts were performed with a pulse-pair resolution of 3.2 ns, and the number of repetitions per pixel producing 0, 1, or more than 1 photons were counted. A maximum likelihood estimator [15] was fit to these counts to infer the photon rate.

2.2 Imaging

Imaging data were collected using a custom-built two-photon microscope incorporating a Chameleon XR Ti: Sapphire laser (Coherent, Santa Barbara, CA) operating at 830 nm and a series of Acousto-Optic deflectors (Isomet, UK) for beam steering. A 60×1.1 NA water objective (Olympus, Japan) was used. Emitted fluorescence was detected with H7422-40 PMT module (Hamamatsu Photonics, Japan). PMT signals were amplified with an adjustable SR570 transimpedance amplifier (Stanford Research Systems, Sunnyvale, CA). Amplifier settings were used that optimize image quality for NND and photocurrent binning experiments. For NND, amplifier was used in 'Low Noise' mode, resulting in a pulse width of 176 μ s. For photocurrent binning, amplifier was set to 'High Bandwidth' mode, resulting in a pulse width of 300 ns. The amplifier used performs near-optimally at these two bandwidths, and the two modes represent the fundamental gain/bandwidth tradeoff of all amplifiers. Signals were inverted and offset by -2 V to avoid saturation, using settings of the amplifier, and were not filtered. Hardware was controlled by, and signals were acquired on, a PCI-6110 DAQ board (National Instruments, Austin, TX) using custom microscopy software written with Matlab and C. Pulse widths (i.e. decay constants) for each amplifier setting were determined by illuminating the PMT with brief pulses of light and measuring decay during the subsequent dark period.

Photocurrent binning images were generated by sampling the detector signal at 2.5 MHz and summing the digitized values within each pixel dwell period (e.g. 2 μ s). For NND images, the digitized signal was first processed by the NND algorithm for the known pulse width (441 samples), and then summed over each pixel dwell period. WD images were generated from the same data as NND images, but were

processed using Wiener Deconvolution. For WD, the signal power spectrum was approximated by assuming a sample autocorrelation coefficient $\rho = 0.4$ (code available upon request). Image intensities were mapped to 16 bit greyscale with the lowest intensity colored black and 1% of pixels saturated. For Figure 5d–f, intensities for all 3 images were multiplied by the same factor to better view dim image regions (some pixels were saturated). To measure fidelity of microscopy images (Figure 5m), images were first aligned to the reference by automated rigid-body registration, and correlation was measured over all pixels present in both the reference and registered test image.

2.3 Animal rearing conditions

Freely-swimming albino *Xenopus laevis* tadpoles were reared in $0.1\times$ Steinberg's solution ($1\times$ Steinberg's in mM: 10 HEPES, 58 NaCl, 0.67 KCl, 0.34 Ca(NO₃)₂, 0.83 MgSO₄, pH 7.4) and housed at room temperature on a 12 hr light/dark cycle. Experiments were conducted with Stage 50 tadpoles in accordance with the Canadian Council on Animal Care guidelines, and were approved by the Animal Care Committee of the University of British Columbia Faculty of Medicine.

2.4 Calcium imaging

Oregon Green BAPTA-1 AM (Molecular Probes, Eugene, OR) was pressure injected into the optic tectum as described previously [24]. 1 hr after injection, tadpoles were placed in a bath containing 4mM pancuronium dibromide for 5 minutes, then placed in a chamber which immobilized the head for imaging. The tadpole tail was perfused with oxygenated $0.1\times$ Steinberg's solution during imaging. The region imaged was roughly 200 μ m below the surface of the tectum. Images were acquired at 10 Hz with a pixel dwell time of 2 μ s. Image registration, ROI selection, spatial filtering, and baseline fitting were performed as described previously to obtain $\Delta F/F_0$ fluorescence traces [6].

3. Results

To compare the effectiveness of NND to established methods, we first simulated imaging using photon counting, photocurrent binning, and NND (Figure 3). Here "images" consisted of random sequences of pixels with intensities uniform randomly distributed

between 0 and a maximum photon rate, which we varied between 6 and 60 photons/pixel. This simulation allowed us to compare the fidelity of the three methods given identical incident photon streams. As an upper bound on possible performance, we also included the theoretical optimal detector limited only by Poisson noise in the photon stream.

At low photon rates, performance is strongly limited by noise in photon counts and even the optimal detector produces images of low fidelity. Photon counting performed nearly as well as the optimal detector at these low rates, peaking in performance in images with a mean rate of 5 photons/ μ s for the detector (Hamamatsu H7421) and sample rates we simulated. Above this rate, photon counting performance decreases as pulses become more likely to overlap in time. Photocurrent binning performs poorly at low rates in comparison to photon counting, but continues to improve as photon rates increase. Photocurrent binning surpassed photon counting in fidelity at a mean photon rate of 4.5 photons/ μ s. NND outperformed photocurrent binning dramatically, producing an improvement in image fidelity equivalent to a 25% increase in the photon rate. NND surpassed photon counting in fidelity at a mean rate of 3 photons/ μ s.

To determine the effect of varying pulse width on performance of NND and photocurrent binning we conducted simulations with a variety of pulse widths (Figure 4a). Photocurrent binning performance peaked at a pulse width of 0.8 samples, and decreased at greater pulse widths, presumably due to increased bleedthrough. NND performance was relatively insensitive to pulse width at widths greater than the sample rate. Both methods showed poor performance at pulse widths much less than the sam-

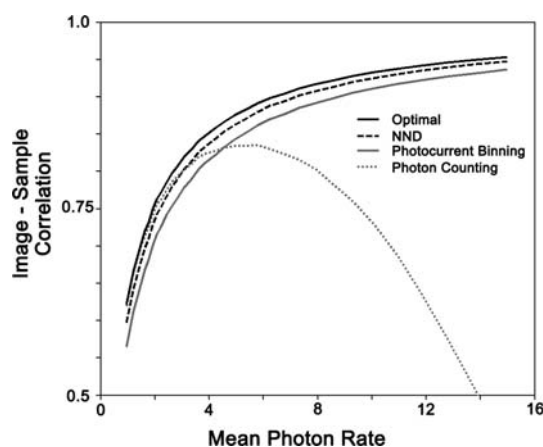


Figure 3 Simulated imaging fidelity as a function of photon rate for different signal processing methods. Fidelity is the correlation between the reconstructed image and original sample intensity, using photon counting (grey dots), photocurrent binning (solid grey), or nonnegative deconvolution (dashes). Also shown is fidelity of the optimal detector, limited only by Poisson noise in photon arrivals (black). Images were composed of random pixels with photon rates uniformly distributed between 0 and twice the indicated mean rate (e.g. for a mean photon rate of 5 photons/pixel, instantaneous rates ranged from 0–10 photons/pixel).

ple rate, indicating decreased apparent quantum efficiency at lower pulse widths.

Well designed imaging systems are typically not limited by noise from sources other than photon counts. However, practical considerations can result in non-negligible measurement noise, and digitization noise in the ADC can affect dim pixels when imaging large dynamic ranges. Taking into account a

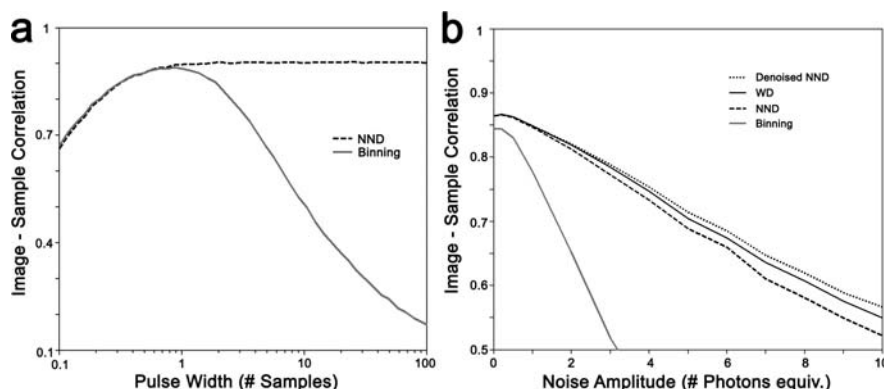


Figure 4 Imaging fidelity of photocurrent binning and NND. **(a)** Imaging fidelity at different pulsewidth/samplerate ratios. At high ratios, photocurrent binning performs poorly due to bleedthrough, which is removed in NND. **(b)** Comparing NND, WD, and Photocurrent Binning at various noise levels. Imaging fidelity of NND (dashes), denoised NND (dots), WD (solid black) and photocurrent binning (solid grey). Noise amplitude is measured in multiples of the mean photon amplitude. WD performs nearly as well as denoised NND, particularly at low measurement noise levels (<1 photon) typical of photomultiplier tubes, though other detectors show higher noise levels. Photocurrent binning performs poorly as noise levels increase.

non-negative constraint on a signal can improve its recovery from noisy measurements [16]. We thus expected NND to perform well in the presence of noise. When spectral properties of the signal and noise are known, NND can be further improved by first applying the optimal denoising filter of Wiener deconvolution. We find this especially relevant when extending the NND method to other problems, such as identifying action potentials in neuronal calcium imaging data [16] (Figure 6). We thus compared the performance of NND, WD, denoised NND, and photocurrent binning at different levels of additive measurement noise (Figure 4b). We find that denoised NND performed best across all noise levels, but that performance of the three deconvolution methods was equivalent at noise levels lower than the amplitude of a single photon pulse. Photocurrent binning performed particularly poorly with increasing additive noise.

We next used a custom-built two-photon microscope to directly compare images produced by each acquisition method. We imaged a sample of auto-fluorescent lily of the valley (*Convallaria sp.*) as a

static specimen. To assess performance of photocurrent binning and NND, we first obtained high fidelity images with each method by averaging 10 frames acquired at a long (12 μ s) pixel dwell time. These images were very similar between the two methods (correlation coefficient $r > 0.997$) and were averaged to produce a reference image (Figure 5a). Single frames were then obtained at a shorter (2 μ s) pixel dwell time using NND and photocurrent binning, and compared to this reference image (Figure 5b, c). These frames were acquired at different intensities of the exciting laser to produce a range of photon detection rates. NND produced higher correlations to the reference than photocurrent binning at all photon rates (Figure 5m). Qualitatively, NND produced visibly less noise in the dimmer parts of the images when viewed at high contrast (Figure 5d–f), resulting in clearer boundaries of dim objects (Figure 5g). Images obtained using photocurrent binning further showed ‘streaking’ bleedthrough artifacts at short pixel dwell times, which were not seen with NND (Figure 5h–l). Images acquired using the same hardware settings as NND but processed using WD

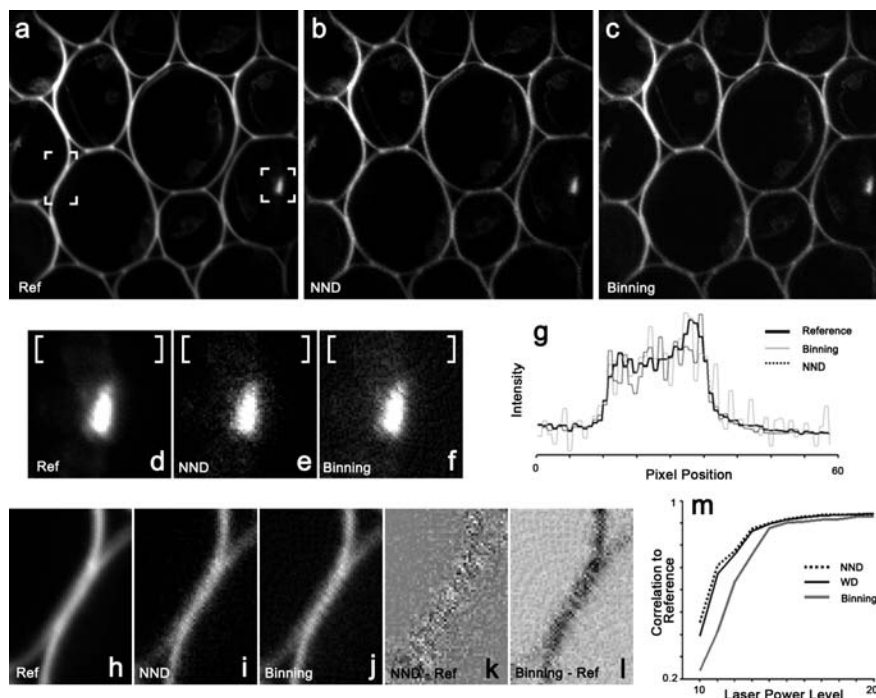


Figure 5 Application of NND to two-photon laser scanning microscopy (a) Reference image of *Convallaria* specimen, the average of images acquired at long pixel dwell time with NND and photocurrent binning (b, c) Images acquired at a 2 μ s pixel dwell time using NND (b) and photocurrent binning (c). White brackets denote regions analyzed in subsequent panels. (d–g) Enlarged region of image. Here, measurement noise has magnitude approaching that of the dimmest detectable objects. NND (e) is insensitive to this noise, producing clearer boundaries for dim objects compared to photocurrent binning (f). Brackets indicate image rows averaged to produce intensity profiles in (g). (h–l) Enlarged region of image. At rapid transitions in pixel brightness, photocurrent binning can produce ‘streaking’ artifacts (j, l) due to bleedthrough, not seen with NND (i, k), or in the reference image (h). Streaking is more clearly seen in difference images (k, l). Scan lines run diagonally (upper left to bottom right) in these images. (m) Imaging fidelity of NND, WD, and photocurrent binning at different excitation laser intensities, with a pixel dwell time of 2 μ s.

showed nearly equivalent performance to NND, without streaking or other imaging artifacts (data not presented).

To assess the performance of NND for rapid quantitative imaging, we performed calcium imaging of spontaneous neuronal activity within the intact brain of awake *Xenopus laevis* tadpoles. Neurons were loaded with Oregon Green Bapta-1 AM (OGB), a dye which increases fluorescence upon binding to Ca^{2+} (Figure 6a). Because the intracellular calcium concentration increases transiently each time a neuron fires an action potential [6], spikes in OGB fluorescence are a marker of neuronal activity. We imaged the same field of neurons at a rate of 10 Hz using photocurrent binning and NND in succession. Imaging with NND resulted in lower noise levels in resulting fluorescence measurements compared to photocurrent binning (Figure 6d), making low amplitude spontaneous spikes, corresponding to 1–3 action potentials [6], more easily detectable (Figure 6b, c). Because neuronal calcium transients show fast onset and exponential decay similar to PMT photon pulses, NND can be used to detect these events [16].

4. Discussion

NND produces higher fidelity images with shorter pixel dwell times than conventional photocurrent binning, and performs near optimally across a greater range of photon rates than commercially available

photon counters. The greatest advantage of NND over photocurrent binning is the absence of bleed-through between adjacent pixels at short pixel dwell times. To avoid this bleedthrough in images acquired with photocurrent binning, the pulse width must be narrowed to a level which reduces effective quantum efficiency. Near-optimal performance at both low and high photon rates make NND well suited for biological imaging applications, where spatial differences in image intensity can be extreme. One such application is single-neuron calcium imaging, where quantitative measurements are made in both the bright neuronal soma and the much dimmer distal dendritic arbor [21, 22]. NND should allow more precise sampling of a greater number of regions of interest for all quantitative imaging applications, facilitating the study of spatially correlated cellular signaling [6].

WD performs nearly as well as NND except at low signal-to-noise ratios. WD can be performed considerably faster than NND, and is therefore well suited for presenting images in real time when multiple channels are being acquired at high sampling rates. In such situations, we use this rapid deconvolution for real-time image presentation, and perform denoised NND offline after acquisition is complete.

For researchers building new microscopes, the preferred detection and processing method for an imaging task depends on the expected photon rates encountered. Analog integration methods (both NND and binning) are most effective at high photon rates. The largest source of error in NND, relative to the optimal detector, is noise due to variability in photon response amplitudes. This variability multi-

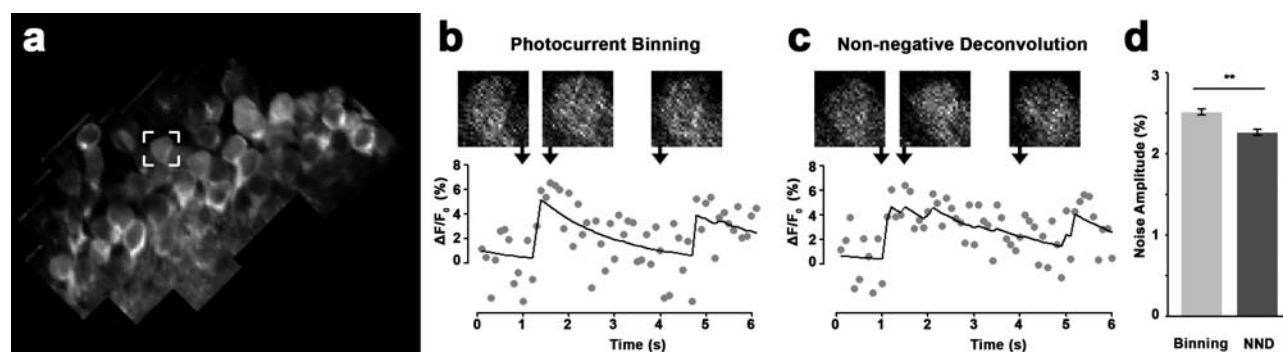


Figure 6 Application of NND to in vivo two-photon calcium imaging. (a) Average intensity projection of a field of neurons loaded with OGB-1, a calcium-sensitive dye, in the optic tectum of a *Xenopus laevis* tadpole. The irregularly shaped imaging area is a random access laser scan; the surrounding black region was not imaged. Here, 49187 pixels were imaged at a dwell time of 2 $\mu\text{s}/\text{pixel}$, at a framerate of 10 Hz. (b, c) (top) Enlarged view of a single neuron (region identified in (a)) at individual timepoints acquired using (b) photocurrent binning or (c) NND. (bottom) Fluorescence intensity ($\Delta F/F_0$) time-courses (gray dots) of spontaneous calcium transients in the same neuron, imaged using (b) photocurrent binning or (c) NND. Traces were acquired 5 minutes apart under identical imaging conditions. Transients in both traces have amplitudes consistent with firing of 1–3 action potentials. Fluorescence timecourses have been fit with NND (black line), demonstrating another application of the algorithm. (d) Standard deviation of residuals after NND fit, in units of $\Delta F/F_0$, for 11 neurons imaged with both photocurrent binning (left) and NND (right). **: $p < 0.01$, paired t -test.

plies the Poisson noise and is therefore strongest relative to the signal at low photon counts. At lower photon rates, photon counting makes more efficient use of photons than NND, because it is nearly immune to noise from pulse height variations. The precise crossover point, where photon counting or analog methods become preferable, depends on several imaging parameters. A recently reported system for two-photon LSM, incorporating novel hardware and processing algorithms for photon counting, increases both the maximum photon count rate and the quality of images formed from those counts [15]. Simulating this method and comparing it to NND, we find a crossover point at a mean photon rate of 42 photons per pixel for pixel dwell times of 2 microseconds (Figure S1). Developments in photodetector technology will continue to improve performance of both analog detection and photon counting methods in the future. Hybrid photodiodes have recently become available with a large active area, excellent gain and quantum efficiencies matching or exceeding that of PMTs, but with much lower pulse height variation (e.g. R10467U-40, Hamamatsu). NND is not strongly affected by the slightly lower gain of these detectors compared to conventional PMTs, and their use should further improve NND performance at low photon rates (Figure S1).

Photon rates can vary considerably across imaging applications. Reasonable non-quantitative images can be generated with an average of 30 photons per pixel, and such images can be acquired relatively quickly at count rates attainable by most photon counting systems. However, accurate quantitative imaging requires many more photons per pixel. Poisson noise in photon arrivals is equal to the square root of the signal amplitude. Measuring the brightness of a pixel to a standard deviation of 10% thus requires detecting a minimum of 100 photons, and determining the ratio of two pixels with this accuracy requires 200 photons per pixel. When the signal being measured varies in time, this large number of photons must be acquired rapidly, making photon counting less effective. For fast imaging, and particularly for fast quantitative imaging, NND performs very well, surpassing existing photon counting and analog methods in fidelity. At lower intensities, photon counting is preferred, particularly when concerns regarding fluorophore bleaching or photodamage dominate. It may also be desirable to image at lower photon rates for experimental reasons, because of limits in dye brightness and the intensity of light that can be used for excitation. Ultimately, the decision to use photon counting or photocurrent measurement depends on the details of the experiments being performed. Hybrid systems which process photon counting and analog signals simultaneously have also been designed [23].

As two-photon and confocal microscopy become more widespread and many researchers develop and build their own microscopes, users have more choice in the methods used to process imaging data. NND can easily be incorporated into existing 'home-built' LSM systems, or to systems using custom software to drive commercial hardware, and in most cases requires no new equipment.

Author biographies Please see Supporting Information online.

References

- [1] M. Chalfie, Y. Tu, G. Euskirchen, W. W. Ward, and D. C. Prasher, *Science* **263**, 802–805 (1994).
- [2] S. Kwok, C. Lee, S. A. Sánchez, T. L. Hazlett, E. Gratton, and Y. Hayashi, *Biochem. Biophys. Res. Commun.* **369**, 519–525 (2008).
- [3] S. X. Chen, P. K. Tari, K. She, and K. Haas, *Neuron* **67**, 967–983 (2010).
- [4] R. M. Hoffman, *BioTechniques* **30**, 1016–1022, 1024–1026 (2001).
- [5] H. Lütcke, M. Murayama, T. Hahn, D. J. Margolis, S. Astori, S. Meyer zum Alten Borgloh, W. Göbel, Y. Yang, W. Tang, and S. Kügler, R. Sprengel, T. Nagai, A. Miyawaki, M. E. Larkum, F. Helmchen, and M. T. Hasan, *Front. Neural Circ.* **4**, doi:10.3389/fncir.2010.00009 (2010).
- [6] K. Podgorski, D. Dunfield, and K. Haas, *PLoS Biol.* **10**, e1001236 (2012).
- [7] J. B. Pawley and B. R. Masters, *J. Biomed. Opt.* **13**, 029902 (2008).
- [8] X. Michalet, F. F. Pinaud, L. A. Bentolila, J. M. Tsay, S. Doose, J. J. Li, G. Sundaresan, A. M. Wu, S. S. Gambhir, and S. Weiss, *Science* **307**, 538–544 (2005).
- [9] B. F. Grewe, D. Langer, H. Kasper, B. M. Kampa, and F. Helmchen, *Nat. Meth.* **7**, 399–405 (2010).
- [10] T. A. Pologruto, B. L. Sabatini, and K. Svoboda, *Biomed. Eng. Online* **2**, doi:10.1186/1475-925X-2-13 (2003).
- [11] A. Majewska, G. Yiu, and R. Yuste, *Pflug. Arch. Eur. J. Physiol.* **441**, 398–408 (2000).
- [12] S. Gomi, H. Hano, T. Iijima, S. Itoh, K. Kawagoe, S. H. Kim, T. Kubota, T. Maeda, T. Matsumura, Y. Mazuka, K. Miyabayashi, H. Miyata, T. Murakami, T. Nakadaira, T. Nakaya, H. Otono, E. Sano, T. Shinkawa, Y. Sudo, T. Takeshita, M. Taguchi, T. Tsubokawa, S. Uozumi, M. Yamaoka, H. Yamazaki, M. Yokoyama, K. Yoshimura, and T. Yoshioka, *Nucl. Instrum. Methods Phys. Res. A* **581**, 427–432 (2007).
- [13] G. N. Gol'tsman, O. Okunev, G. Chulkova, A. Lipatov, A. Semenov, K. Smirnov, B. Voronov, A. Dzardanov, C. Williams, and R. Sobolewski, *Appl. Phys. Lett.* **79**, 192–195 (2001).
- [14] Z. L. Yuan, B. E. Kardynal, A. W. Sharpe, and A. J. Shields, *Appl. Phys. Lett.* **91**, 041114-1–041114-3 (2007).

- [15] J. D. Driscoll, A. Y. Shih, S. Iyengar, J. J. Field, G. A. White, J. A. Squier, G. Cauwenberghs, and D. Kleinfeld, *J. Neurophysiol.* **105**, 3106–3113 (2011).
- [16] J. T. Vogelstein, A. M. Packer, T. A. Machado, T. Sippy, B. Babadi, R. Yuste, and L. Paninski, *J. Neurophysiol.* **104**, 3691–3704 (2010).
- [17] Yuanqing Lin, D. D. Lee, and L. K. Saul, *Proc. IEEE Int. Conf. Acoust. Speech Signal Process.* **2**, 377–380 (2004).
- [18] L. K. Saul, F. Sha, and D. D. Lee, in: 8th European Conference on Speech Communication and Technology, Geneva, Switzerland, September 1–4, 2003, p. 35.
- [19] N. Wiener, *Extrapolation, interpolation, and smoothing of stationary time series*. (MIT Press, Cambridge, MA 1949).
- [20] M. Frigo, S. G. Johnson, *Proc. IEEE Int. Conf. Acoust. Speech Signal Process.* 1381–1384 (1998).
- [21] T. Nevian and F. Helmchen, *Pflug. Arch. Europ. J. Physiol.* **454**, 675–688 (2007).
- [22] J. H. Bollmann and F. Engert, *Neuron* **61**, 895–905 (2009).
- [23] R. K. Newsom, D. D. Turner, B. Mielke, M. Clayton, R. Ferrare and C. Sivaraman, *Appl. Opt.* **48**, 3903–3914 (2009).
- [24] D. Dunfield and K. Haas, *Neuron* **64**, 240–250 (2009).

No small Matter

Micro and Nano:

For subscription details please contact Wiley Customer Service:

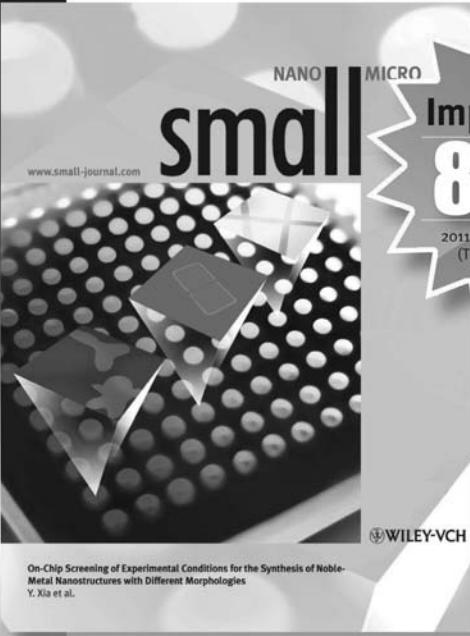
>> cs-journals@wiley.com
(Americas, Europe, Middle East and Africa, Asia Pacific)

>> cs-germany@wiley.com
(Germany, Austria, Switzerland)

>> cs-japan@wiley.com
(Japan)

WILEY

WILEY-VCH



2012. Volume 8, 24 issues.
Print ISSN 1613-6810 / Online ISSN 1613-6829

For more information please visit
www.small-journal.com
or contact us at small@wiley-vch.de

Impact Factor
8.349
2011 Journal Citation Reports®
(Thomson Reuters, 2012)

provides the very best forum for experimental and theoretical studies of fundamental and applied interdisciplinary research at the micro- and nanoscales

4528511207_bu